High-resolution Transmission Spectra of Earth Through Geological Time

Lisa Kaltenegger[1,2] , Zifan Lin[1,2] , and Jack Madden[1,2]
[1] Cornell University, Astronomy and Space Sciences Building, Ithaca, NY 14850, USA
[2] Carl Sagan Institute, Space Science Building 311, Ithaca, NY 14850, USA
Received 2019 December 14; revised 2020 February 10; accepted 2020 February 11; published 2020 March 26

Abstract

The next generation of ground- and space-based telescopes will be able to observe rocky Earth-like planets in the near future, transiting their host star. We explore how the transmission spectrum of Earth changed through its geological history. These transmission spectra provide a template for how to characterize an Earth-like exoplanet— from a young prebiotic world to a modern Earth. They also allow us to explore at what point in its evolution a distant observer could identify life on our *Pale Blue Dots* and other worlds like it. We chose atmosphere models representative of five geological epochs of Earth's history, corresponding to a prebiotic high CO_2-world 3.9 billion years ago (Ga), an anoxic world around 3.5 Ga, and 3 epochs through the rise of oxygen from 0.2% to present atmospheric levels of 21%. Our transmission spectra show atmospheric spectral features, which would show a remote observer that Earth had a biosphere since about 2 billion years ago. The high-resolution transmission spectral database of Earth through geological time from the VIS to the IR is available online and can be used as a tool to optimize our observation strategy, train retrieval methods, and interpret upcoming observations with the James Webb Space Telescope, the Extremely Large Telescopes, and future mission concepts like Origins, HabEx, and LUOVIR.

1. Introduction

Among the more than 4000 discovered exoplanets to date are dozens of Earth-size planets (see, e.g., Udry et al. 2007; Borucki et al. 2011, 2013; Kaltenegger & Sasselov 2011; Batalha et al. 2013; Kaltenegger et al. 2013; Quintana et al. 2014; Torres et al. 2015), including several with similar irradiation to Earth (see, e.g., Kane et al. 2016; Kaltenegger 2017; Berger et al. 2019; Johns et al. 2018).

The space-based James Webb Space Telescope (JWST) is scheduled to launch in early 2021 and several ground-based Extremely Large Telescopes (ELTs) are currently under construction or in planning, like the Giant Magellan Telescope, the Thirty Meter Telescope, and the ELT, which are designed to be able to undertake the first measurements of the atmospheres of Earth-sized planets (see, e.g., Kaltenegger & Traub 2009; Kaltenegger et al. 2010, 2019; Garcõa Munoz et al. 2012; Hedelt et al. 2013; Snellen et al. 2013; Betremieux & Kaltenegger 2014; Misra et al. 2014; Rodler & Lopez-Morales 2014; Barstow et al. 2016; Stevenson et al. 2016; Lin & Kaltenegger 2019). Several future mission concepts like Origins (Battersby et al. 2018), Habex (Mennesson et al. 2016), and LUOVIR (LUOVIR Team 2018) are currently being designed to be able to explore the atmospheric composition of Earth-sized planets.

Earth's atmosphere has undergone a substantial evolution since formation (see, e.g., Walker 1977; Zahnle et al. 2007; Lyons et al. 2014). Previous work by one of the authors modeled Earth's reflection and emission spectra through geological time, representative of exoplanet observations seen as directly imaged *Pale Blue Dots* (Kaltenegger et al. 2007). A second paper including one of the authors investigated how the reflection and emission spectra of Earth through its geological history from anoxic to modern Earth-like planets changes if

they are orbiting different Sun-like host stars from F0V to M8V spectral type (Rugheimer & Kaltenegger 2018). The surface UV environment for Earth through geological time for our Sun and around different Sun-like host stars shows comparable UV surface environments for such planets as discussed in Rugheimer & Kaltenegger (2018), O'Malley-James & Kaltenegger (2017), and O'Malley-James & Kaltenegger (2019).

While emission and reflection spectra for models of Earth through geological time exist (e.g., Kaltenegger et al. 2007; Rugheimer & Kaltenegger 2018), transmission spectra have been focused on modern Earth so far (see, e.g., Ehrenreich et al. 2006; Kaltenegger & Traub 2009; Palle et al. 2009; Vidal-Madjar et al. 2010; Rauer et al. 2011; Garcõa Munoz et al. 2012; Betremieux & Kaltenegger 2013, 2014; Hedelt et al. 2013; Misra et al. 2014). Here we model the high-resolution transmission spectra for five geological epochs in Earth's history (Table 1): representative of a high-CO_2 prebiotic world as epoch 1 around 3.9 Ga, an Anoxic world as epoch 2 around 3.5 Ga and 3 epochs during the rise of oxygen, corresponding to the timeframe of the rise of oxygen in Earth's atmosphere between about 2.4 Ga to today (see review by Lyons et al. 2014). We modeled epoch 3 after the Grand Oxygenation Event, with 1% present atmospheric levels (PALs) of O_2, epoch 4 after the Neoproterozoic Oxygenation Event, with 10% PAL O_2. Epoch 5 represents modern Earth atmosphere with 21% O_2. We use a solar evolution model (Claire et al. 2012) to establish the incident Solar Flux through Earth's geological evolution. All our models assume a planet with the same radius and mass as Earth which orbits at 1 au from an evolving Sun.

Our high-resolution database of transmission spectra from the visible to the Infrared (0.4–20 μm) for Earth through geological time, which is freely available online (www.carlsaganinstitute.org/data), is a tool to enable effective observations and first interpretation of atmospheric spectra of

Table 1
Chemical Mixing Ratios for Major Atmospheric Gases in our Model Atmospheres, for Five Epochs through Earth's Geological History from Prebiotic to Anoxic Atmospheres Representative of 3.9 and 3.5 Ga in Earth's History to Three Models which Capture the Rise of Oxygen from a Neoproterozoic Earth Modeled with 0.01PAL O_2 to Modern Earth with 21% O_2

Time Period	Solar Constant	Epoch	CO_2	CH_4	O_2	O_3	N_2O
Now	1.00	5	3.65E−04	1.65E−06	2.10E−01	3.00E−08	3.00E−07
0.5−0.8	0.95	4	1.00E−02	4.15E−04	2.10E−02	2.02E−08	9.15E−08
1.0−2.0	0.87	3	1.00E−02	1.65E−03	2.10E−03	7.38E−09	8.37E−09
3.5	0.77	2	1.00E−02	1.65E−03	1.00E−13	2.55E−19	0
3.9	0.75	1	1.00E−01	1.65E−06	1.00E−13	2.55E−19	0

Earth-like planets, using our planet's evolution as a template. Our models and transit spectra include climate indicators like H_2O and CO_2 as well as biosignatures like the combination of O_2 or O_3 in combination with a reduced gas like CH_4 (see discussion on biosignatures, e.g., in Kaltenegger 2017). The term biosignatures is used here to mean remotely detectable atmospheric gases that are produced by life and are not readily mimicked by abiotic processes, e.g., the CH_4 + O_2 (Lederberg 1965; Lovelock 1965) or CH_4 + N_2O (Lippincott et al. 1967) pairs.

In Section 2 we describe our model. In Section 3 we present the transmission spectra for five epochs in Earth's geological history and discuss the absorption features of climate indicators and biosignatures in low- and high-resolution from the visible to infrared wavelength. Section 4 discusses and summarizes our results.

2. Methods

We used EXO-Prime (for details, see Kaltenegger et al. 2007; Kaltenegger & Sasselov 2010 and Madden & Kaltenegger 2020) to simulate Earth's atmosphere and transmission spectra for five geological epochs. EXO-Prime is a coupled 1D iterative climate-photochemistry code (see, e.g., Kasting & Ackerman 1986; Pavlov & Kasting 2002; Segura et al. 2005, 2007; Haqq-Misra et al. 2008; Arney et al. 2016; Madden & Kaltenegger 2020), with a line by line Radiative Transfer code (e.g., Traub & Stier 1976; Kaltenegger & Traub 2009) for rocky exoplanets, which was originally developed for Earth. EXO-Prime has been validated for visible to infrared wavelengths by comparison to Earth observed as an exoplanet from different missions like *EPOXI*, the *Mars Global Surveyor*, Shuttle data, and multiple earthshine observations (Kaltenegger et al. 2007; Kaltenegger & Traub 2009; Rugheimer et al. 2013).

We calculate the high-resolution transmission spectra at a resolution of $0.01\,cm^{-1}$ using opacities from the 2016 HITRAN database (Gordon et al. 2017) for O_2, O_3, H_2O, CO_2, CH_4, N_2O, CH_3Cl, SO_2, H_2S, H_2O_2, OH, HO_2, HOCl, H_2CO, HCl, ClO, NO_2, NO, HNO_3, and CO. For $CFCl_3$ (Sharpe et al. 2004) and N_2O_5 (Wagner & Birk 2003) we use cross-sections. We include CO_2 line mixing (see also Niro et al. 2005a, 2005b). For CO_2, H_2O, and N_2, we use measured continua data instead of line-by-line calculations in the far wings (see Traub & Jucks 2002). Earth's atmosphere cannot be probed in primary transit below 12 km, because refraction from the deeper atmospheric regions deflects light away from a distant observer in an Earth–Sun geometry (see, e.g., Garcõa Munoz et al. 2012; Betremieux & Kaltenegger 2014; Misra et al. 2014). Our transmission spectra show the cutoff due to

refraction at 12 km for all epochs. Clouds do not significantly affect the strengths of the spectral features in Earth's transmission because most clouds on Earth are located at altitudes below 12 km.

The dominant contributions to transmission spectra from Earth-like planet atmospheres come from the atmosphere below 60 km in the wavelength range modeled, and so we model our atmospheres to approximately 60 km (10^{-4} bar). This does not influence the spectra because of the low density of the model atmosphere above that height. However outside the considered wavelength range, higher parts of the atmosphere can contribute significantly to the transmission spectra, like shown for modern Earth's UV transmission spectrum (Betremieux & Kaltenegger 2014).

We base the transmission spectra for Earth through geological times on atmosphere models by Kaltenegger et al. (2007) and Rugheimer & Kaltenegger (2018): The models for each epoch are discussed in detail in those two papers and summarized in Table 1 and Figure 1. The changing solar constant accounts for the lower solar incident flux at earlier times in Earth's history, following the prediction of a 30% reduction in solar flux for a young Earth at 4.6 Ga (Claire et al. 2012). All our models assume Earth-radius and -mass and a planet that orbits at 1 au around an evolving Sun. All epochs assume a 1 bar surface pressure, consistent with geological evidence for paleo-pressures close to modern values (e.g., Som et al. 2012; Marty et al. 2013).

Epoch 1 is a CO_2-rich atmosphere of a prebiotic world, representative of early Earth around 3.9 Ga. Epoch 2 is an Archaen world, representative of a young Earth around 3.5 Ga. Epoch 3 corresponds to a Paleo- and Meso-proterozoic Earth (about 2–1 Ga), when oxygen started to rise in Earth's atmosphere. We use 0.21% O_2 (1% PAL) for this model. Epoch 4 corresponds to the proliferation of multicellular life on Neoproterozoic Earth (about 0.8–0.5 Ga) when the oxygen concentration had risen to 10% PAL (2.1% O_2). Epoch 5 corresponds to modern Earth with 21% O_2. Note that the time of the oxygen rise has recently been moved to a later stage in Earth's evolution (see, e.g., the review in Lyons et al. 2014), which is reflected in the time ranges gives in Table 1 for epoch 3 and epoch 4, instead of geological times given in our earlier paper (Kaltenegger et al. 2007), which based O_2 concentrations on work by Holland (2006).

The transmission spectra in Figure 2 are smoothed with a triangular kernel to a resolving power of 700 for clarity. We did not add noise to the spectra to provide theoretical input spectra for several instruments, which all have different instrument-specific noise profiles that can easily be added to our model to provide realistic observation simulations.
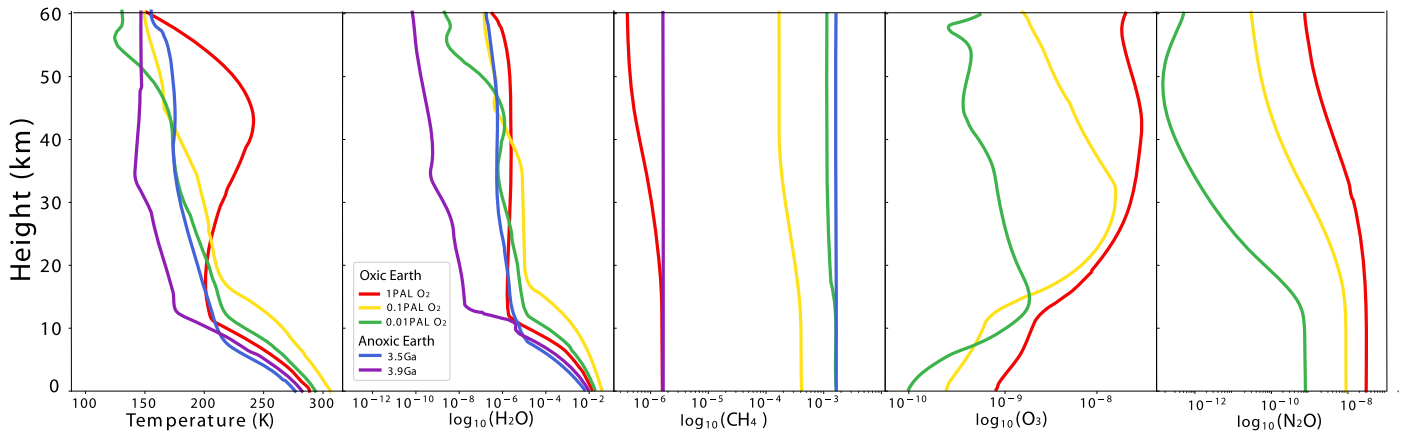
Figure 1. Temperature and mixing ratios for major atmospheric gases in our model atmospheres, representative of five epochs through Earth's geological evolution from an CO_2-rich prebiotic atmosphere around 3.9 Ga to an anoxic atmosphere around 3.5 Ga and three models that capture the rise of oxygen from 0.01PAL O_2 for a Neoproterozoic Earth to 1PAL (21% O_2) on modern Earth. The mixing ratios shown (left to right) are H_2O, CH_4, O_3, and N_2O (see also Table 1).

3. Results

All transmission spectra are available online for a minimum resolution of $\lambda/\Delta\lambda > 100{,}000$ for the full wavelength range from 0.4 to 20 μm (0.01 cm^{-1} steps). Figure 2 shows the transmission spectra for a resolution of $\lambda/\Delta\lambda = 700$ for clarity, with the most prominent spectral features identified. The five atmosphere models are representative of Earth through geological time sorted from modern Earth on top to early Earth on the bottom.

Modern Earth's transmission spectrum is shown as the top row (Epoch 5, 21% O_2), followed by the transmission spectrum for Neoproterozoic Earth (Epoch 4, 0.5–0.8 Ga, $O_2 = 2.1 \times 10^{-2}$ (10% PAL)), followed by the transmission spectrum for a Paleo- and Meso-proterozoic Earth (Epoch 3, 1 to 2 Ga, $O_2 = 2.1 \times 10^{-3}$ (1% PAL)), an anoxic Earth (Epoch 2, 3.5 Ga) and a prebiotic Earth (epoch 1, 3.9 Ga), which is shown in the bottom row.

Throughout the atmospheric evolution of our Earth model, different absorption features dominate Earth's spectrum. CH_4 and CO_2 absorption dominants in the modeled wavelength range for early Earth models. O_2 and O_3 feature an increase in strength with O_2 abundance from a Paleo- and Meso-proterozoic Earth in epoch 3 to modern Earth in epoch 5. Table 1 summarizes the mixing ratios for the dominant chemicals in the atmosphere models for the different epochs (see Rugheimer & Kaltenegger 2018). The specific wavelengths where the absorption features can be seen in transmission in Figure 2 are summarized by wavelength below in detail.

Note that while several features overlap at the resolution of $\lambda/\Delta\lambda = 700$, which is shown in Figure 2 for clarity and are not specifically labeled. In the high-resolution online transmission spectra additional individual spectral lines can be easily discerned for these molecules, as shown in Figure 3 for O_2 and O_3 for biotic atmospheres (epoch 5 to epoch 3), for a resolution of $\lambda/\Delta\lambda = 100{,}000$ as proposed for several instruments on the ELTs.

Absorption features in the visible wavelength range (left panel, 0.4–2 μm): Modern Earth (epoch 5, top row) shows a strong absorption feature for O_2 at 0.76 μm, with a weaker feature at 0.69 μm. O_3 shows a broad feature, from approximately 0.45 to 0.74 μm. These features decrease with decreasing oxygen composition for younger Earth models

and disappear for anoxic Earth atmosphere models (epoch 1 and epoch 2). CH_4 in modern Earth's atmosphere shows no significant absorption features in transmission in the visible in Figure 2, but at higher abundance, it shows absorption features at 1.7, and also at 0.88 and 1.4 μm in earlier Earth models. H_2O shows absorption features at a wide range of wavelengths in the visible at 0.73, 0.82, 0.95, and 1.4 μm. CO_2 does not show visible features at present abundance, but in a high-CO_2 atmosphere of 10% CO_2, as in early Earth evolution stages, the weak 1.6 and 2 μm features can be seen in Figure 2.

Absorption features in the NIR wavelength range (middle panel from 2 to 5 μm): Neither O_2 nor O_3 show absorption features in the NIR. CH_4 shows absorption features at 2.4 and 3.3 μm, which increase with CH_4 abundance in Earth's atmosphere for earlier geological epochs. Several CO_2 features can be identified in Figure 2 with increasing CO_2 abundance for younger Earth models. H_2O abundance and absorption feature strength increase with increasing surface temperature and consequent evaporation rate for epoch 3 and epoch 4. The transmission spectra for epochs 2 to 4 are similar in the NIR because they are dominated by CO_2 and CH_4 absorption features. The CO_2 mixing ratio for these epochs is constant and the CH_4 mixing ratio only increases slightly from epochs 2 to 4 (see Table 1).

Absorption in the IR wavelength range (right panel from 5 to 20 mm): At 9.6 μm the strength of the absorption feature of O_3 decreases with decreasing O_3 abundance for younger oxic Earths. It is a saturated feature and therefore an excellent qualitative but poor quantitative indicator for the existence of O_2. A smaller O_3 feature can be seen at 9 μm also decreasing in strength with decreasing O_3 abundance. For anoxic atmospheres the O_3 feature is not visible. At 7.6 μm the absorption feature of CH_4 becomes stronger with increasing CH_4 abundance for younger Earth models. The main CO_2 feature at 15 μm as well as several smaller CO_2 features at 10.4 and 9.4 μm increase with increasing CO_2 abundance for earlier Earth models. H_2O features can be seen at 7 and 20 μm. N_2O has a spectral feature at 16.89 μm, which can be seen in epochs 3 to 5 in the wing of the 15 μm CO_2 feature at the resolution shown in Figure 2.

Note that in the online high-resolution transmission spectra many absorption features, which are not apparent in Figure 2 at a resolution of $\lambda/\Delta\lambda = 700$, can be identified. As an example we show the change in both the O_2 feature at 0.76 μm and the
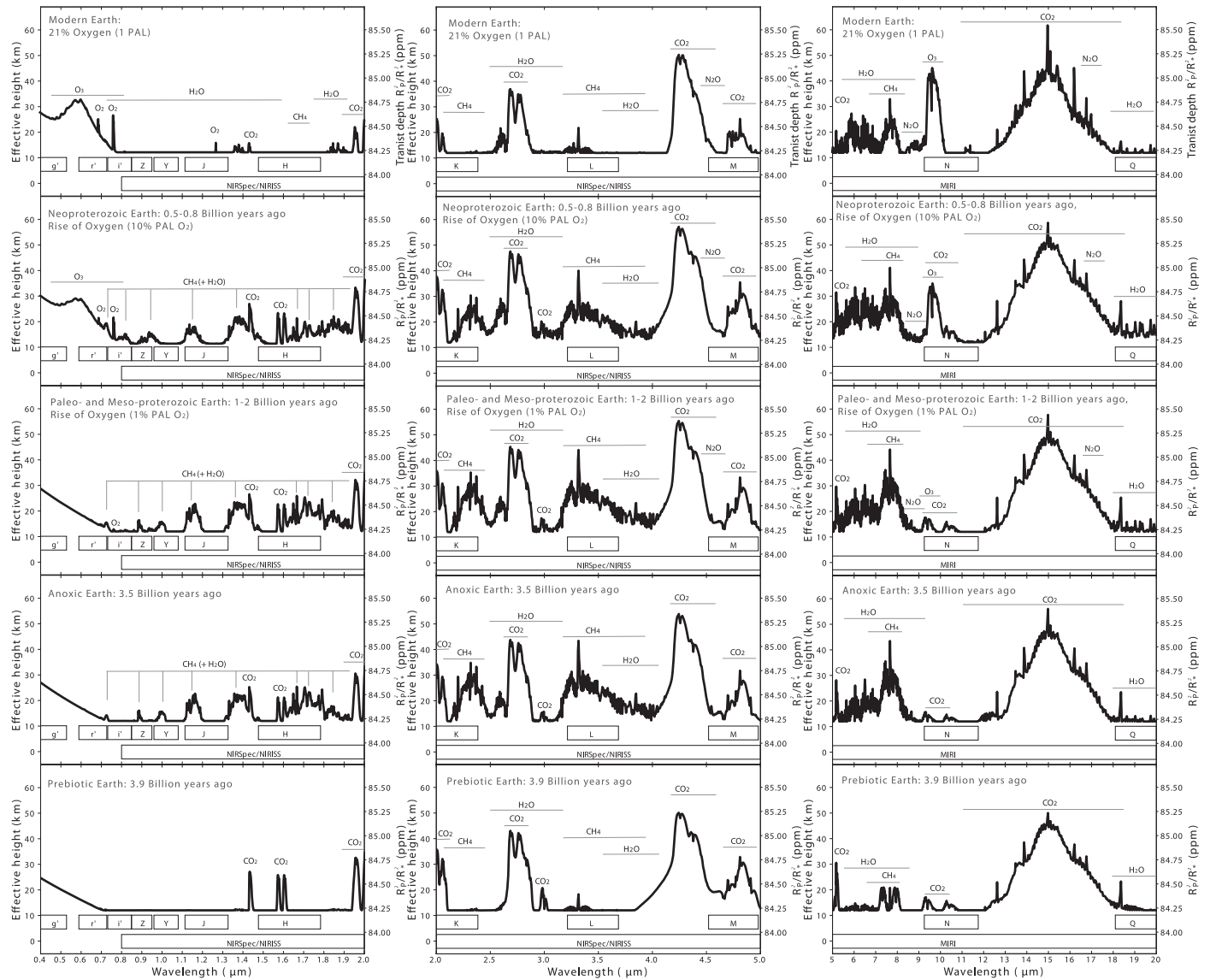
Figure 2. Model spectra for Earth through geological time from 0.4 to 20 μm shown at a resolution of $\lambda/\Delta\lambda = 700$ for five epochs through Earth's geological time from a prebiotic atmosphere 3.9 billion years ago (Ga) to an anoxic atmosphere around 3.5 Ga and 3 models that capture the rise of oxygen, which started around 2.4 Ga, from a Neoproterozoic Earth with 0.01 PAL O_2 to modern Earth with 1PAL (21% O_2).

(The data used to create this figure are available.)

O_3 feature at 9.6 μm through geological time in Figure 3 from a Neoproterozoic Earth model with 0.01 PAL of O_2, Paleo- and Meso-proterozoic Earth modeled with 0.1 PAL O_2 and modern Earth with 21% O_2 for a minimum resolution of $\lambda/\Delta\lambda = 100,000$ for the whole wavelength range shown. N_2O has spectral features at 16.89 μm, which can be seen in epochs 3 to 5 in the wing of the 15 μm CO_2 feature at the resolution shown in Figure 2. The smaller N_2O features at 7.75, 8.52, and 10.65 μm, which overlap with other spectral features at the resolution shown in Figure 2, require high-resolution to be distinguishable.

Many spectral features as well as the differences between epochs are clear at high resolution. However, the increased observing time required to collect high-resolution spectra introduces a trade-off between resolution and observing time, which is instrument specific and depends among other factors on telescope size, observing conditions (ground-based versus

space-based), specific instruments, detectors, and background noise, and is not discussed here. The *y*-axis on the right in Figure 2 shows the transit depth. The spectral features shown correspond to transit depth changes of around 1 ppm for a host star the size of the Sun. However, for smaller host stars the transit depth increases by up to two orders of magnitude. For specific instruments and proposed instrument designs for different ground- and space-based telescopes several teams have run such simulations (see, e.g., Snellen et al. 2013; Rodler & Lopez-Morales 2014; Barstow & Irwin 2016; Stevenson et al. 2016).

Our spectral database provides noise-free high-resolution spectra to optimize observation strategies for different instruments, as well as train retrieval methods and interpret upcoming observations with JWST, the Extremely Large Telescopes, and future mission concepts like Origins, HabEx, and LUOVIR.
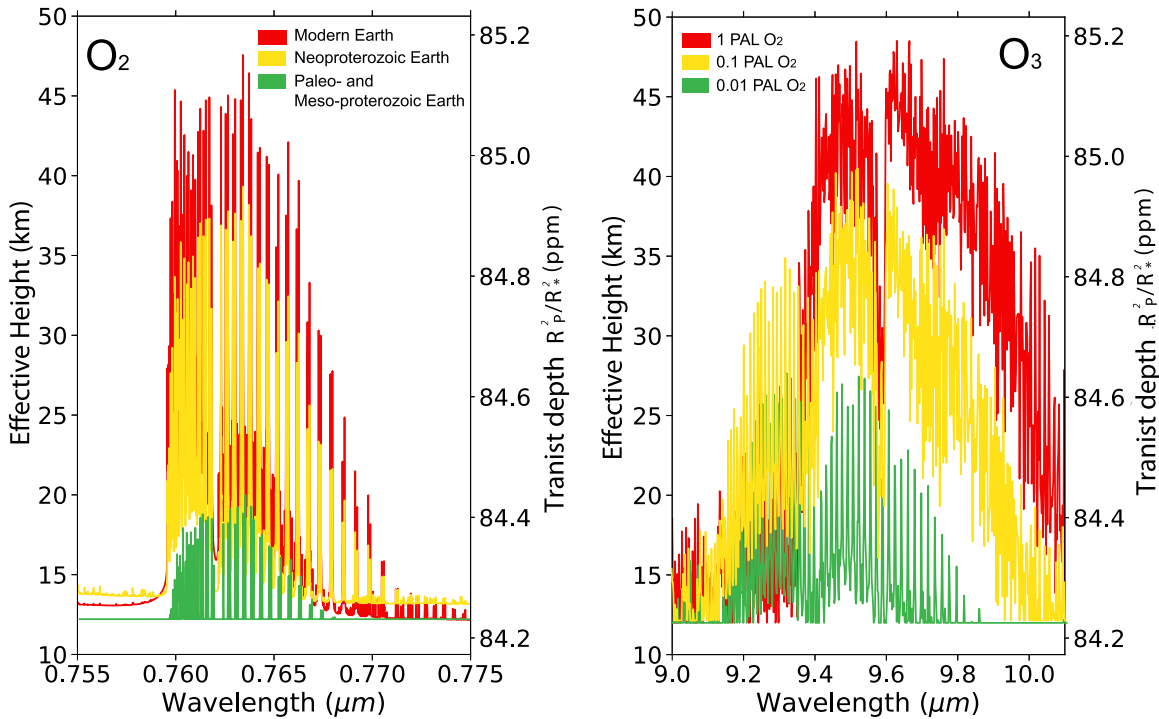
Figure 3. High-resolution ($\lambda/\Delta\lambda > 100,000$) for the 0.76 μm O_2 (left) and 9.6 μm O_3 (right) feature for the rise of oxygen from a Neoproterozoic Earth model with 0.01 present atmospheric level (PAL) of O_2, Paleo- and Meso-proterozoic Earth modeled with 0.1 PAL O_2 and modern Earth with 21% O_2.

Discussion on the detectability of biosignatures through Earth's geological evolution: Analyzing the emergent spectrum of Earth, taken by the Galileo probe, Sagan et al. (1993) concluded that the large amount of O_2 in the presence of CH_4 is strongly suggestive of biology, as Lovelock (1965) and Lederberg (1965) suggested earlier. On short timescales, the two species react to produce CO_2 and H_2O and therefore, must be constantly replenished to maintain detectable concentrations. It is their quantities and detection along with other atmospheric species in the planetary context that solidify a biological origin (as discussed in detail in several recent reviews, e.g., Kasting et al. 2014; Kaltenegger 2017; Swieterman 2018). In the transmission spectra for Earth through geological time, the combination of the strongest absorption bands of CH_4 (7.6 μm, 2.4 μm and several absorption features in the visible for higher CH_4 concentration for Neoproterozoic and younger Earth models) and O_2 (0.76 μm) or O_3 (9.6 and 0.6 μm) gases can be detected at several different wavelengths, dependent on their abundance, Earth's geological evolution, and the spectral resolution.

Figure 2 shows a resolution of $\lambda/\Delta\lambda = 700$, where for epoch 5 (modern Earth) and epoch 4 (Paleo- and Meso-proterozoic Earth), the absorption features of O_2 in the visible at 0.76 μm, CH_4 in the NIR at 2.4 μm and in the IR at 7.6 μm, and O_3 in the IR at 9.6 μm can be clearly seen. Note that in the visible where H_2O and CH_4 features overlap, CH_4 features become the dominant feature in transmission for higher CH_4 concentrations for Neoproterozoic and earlier Earth models.

The O_2 and O_3 absorption features for modern Earth are stronger as the absorption feature decreases with decreasing amount of oxygen in the atmosphere. Figure 2 shows that for epoch 3 (Neoproterozoic Earth model), the oxygen concentration is too low to be able to identify the O_2 and O_3 features in the visible. The O_3 feature in the IR also becomes hard to distinguish. High-resolution spectra, however, allow us to

identify the O_2 as well as O_3 features (see Figure 3) for a minimum resolution of $\lambda/\Delta\lambda = 100,000$. Note that many other spectral features like N_2O features at 7.75, 8.52, and 10.65 μm, which overlap with other spectral features at the resolution shown in Figure 2, require high-resolution to be distinguishable for modern Earth to Neoproterozoic Earth (see high-resolution spectra online).

4. Conclusion

We generated a high-resolution transmission spectral database of atmospheric models representative of Earth through its geological history from the VIS to the IR (0.4–20 μm) with a minimum resolution of 100,000. These transmission spectra provide a template of how to remotely characterize Earth through its geological evolution at 1 au from our Sun- as well as Earth-like exoplanets with upcoming ground- and space-based telescopes and explore at what point in its evolution a distant observer could identify life on our own planet and others like it.

We chose atmospheres representative of five geological epochs of Earth's history, corresponding to a prebiotic high CO_2-world and an anoxic world at 3.9 and 3.5 billion years ago, as well as three epochs through the rise of O_2 from 1% of to present atmospheric levels, which started 2.4 billion years ago on Earth. Throughout the atmospheric evolution of our Earth, different absorption features dominate Earth's transmission spectrum (shown in Figure 2 at a resolution of $\lambda/\Delta\lambda = 700$) with CH_4 and CO_2 being dominant in early Earth models, where they are more abundant. O_2 and O_3 spectral features become stronger with increasing abundance during the rise of oxygen (Epoch 3–5). High-resolution ($\lambda/\Delta\lambda = 100,000$) spectral features that indicate life on Earth —the combination of O_2 or O_3 with a reducing gas like CH_4 or N_2O—can be detected for oxygen levels as low as 0.01 present

atmospheric levels (0.21% O_2), which correspond to a Neoproterozoic Earth model and a time about one to two billion years ago in Earth's history. For lower resolution (example of $\lambda/\Delta\lambda = 700$ in Figure 2) the O_2 and O_3 features only become distinguishable for concentrations of 10% PAL O_2 levels, which corresponds to Paleo- and Meso-proterozoic Earth about 800–500 million years ago.

The high-resolution transmission spectra database ($\lambda/\Delta\lambda > 100{,}000$) is available online www.carlsaganinstitute.org/data and can be used as a tool to optimize our observation strategy, train retrieval methods, and interpret upcoming observations with *JWST* as well as ground-based Extremely Large Telescopes and future mission concepts like Origins, HabEx, and LUOVIR.

ORCID iDs

Lisa Kaltenegger ⑩ https://orcid.org/0000-0002-0436-1802
Zifan Lin ⑩ https://orcid.org/0000-0003-0525-9647
Jack Madden ⑩ https://orcid.org/0000-0002-4701-7833

References

Arney, G., Domagal-Goldman, S. D., Meadows, V. S., et al. 2016, AsBio, 16, 873
Barstow, J. K., & Irwin, P. G. J. 2016, MNRS Lett, 461, L92
Batalha, N. M., Rowe, J. F., Bryson, S. T., et al. 2013, ApJS, 204, 24
Battersby, C., Armus, L., Bergin, E., et al. 2018, NatAs, 2, 596
Berger, T. A., Huber, D., Gaidos, E., & van Saders, J. L. 2018, ApJ, 866, 99
Betremieux, Y., & Kaltenegger, L. 2013, ApJL, 772, L31
Betremieux, Y., & Kaltenegger, L. 2014, ApJ, 791, 7
Borucki, W. J., Agol, E., Fressin, F., et al. 2013, Sci, 340, 587
Borucki, W. J., Koch, D. G., Basri, G., et al. 2011, ApJ, 736, 19
Claire, M. W., Sheets, J., Cohen, M., et al. 2012, ApJ, 757, 95
Ehrenreich, D., & Tinetti, G. 2006, A&A, 448, 379
Garcõa Munoz, A., Zapatero Osorio, M. R., Barrena, R., et al. 2012, ApJ, 755, 103
Gordon, I.E., Rothman, L.S., Hill, C., et al. 2017, JQSRT, 203, 3
Haqq-Misra, J. D., Domagal-Goldman, S. D., Kasting, P. J., & Kasting, J. F. 2008, AsBio, 8, 1127
Hedelt, P., von Paris, P., Godolt, M., et al. 2013, A&A, 553, A9
Holland, R. 2006, RSPTB, 361, 903
Johns, D., Marti, C., Huff, M., et al. 2018, ApJS, 239, 1
Kaltenegger, L. 2017, ARA&A, 55, 433
Kaltenegger, L., Henning, W. G., & Sasselov, D. D. 2010, AJ, 140, 1370
Kaltenegger, L., Madden, J., Lin, Z., et al. 2019, ApJL, 883, 2
Kaltenegger, L., & Sasselov, D. D. 2010, ApJ, 708, 1162
Kaltenegger, L., & Sasselov, D. D. 2011, ApJL, 736, L25
Kaltenegger, L., Sasselov, D., & Rugheimer, S. 2013, ApJL, 775, L47
Kaltenegger, L., & Traub, W. A. 2009, ApJ, 698, 519
Kaltenegger, L., Traub, W. A., & Jucks, K. W. 2007, AJ, 658, 598
Kane, S. R., Hill, M. L., Kasting, J. F., et al. 2016, ApJ, 830, 1
Kasting, J. F., & Ackerman, T. P. 1986, Sci, 234, 1383
Kasting, J. F., Kopparapu, R., Ramirez, R. M., & Harman, C. E. 2014, PNAS, 111, 12641
Lederberg, J. 1965, Natur, 207, 9
Lin, Z., & Kaltenegger, L. 2020, MNRAS, 491, 2845
Lippincott, E. R., Eck, R. V., Dayhoff, M. O., & Sagan, C. 1967, ApJ, 147, 753
Lovelock, J. E. 1965, Natur, 207, 568
LUOVIR Team 2018, arXiv:1809.09668
Lyons, T. W., Reinhard, T. W., & Planavsky, N. J. 2014, Natur, 506, 307
Madden, J., & Kaltenegger, L. 2020, MNRAS, in press
Marty, B., Zimmermann, L., Pujol, M., Burgess, R., & Philippot, P. 2013, Sci, 342, 101
Mennesson, B., Gaudi, S., Seager, S., et al. 2016, Proc. SPIE, 9904, 99040L
Misra, A., Meadows, V., Claire, M., & Crisp, D. 2014, AsBio, 14, 67
Niro, F., Jucks, K., & Hartmann, J.-M. 2005a, JQSRT, 95, 469
Niro, F., Von Clarmann, T., Jucks, K., & Hartmann, J.-M. 2005b, JQSRT, 90, 61
O'Malley-James, J. T., & Kaltenegger, L 2019, MNRAS, 485, 5598
O'Malley-James, J. T., & Kaltenegger, L. 2017, MNRS Lett, 469, L26
Palle, E., Osorio, M. R. Z., Barrena, R., et al. 2009, Natur, 459, 814
Quintana, E. V., Barclay, T., Raymond, S. N., et al. 2014, Sci, 344, 277
Rauer, H., Gebauer, S., Paris, P. V., et al. 2011, A&A, 529, A8
Rodler, F., & Lopez-Morales, M. 2014, ApJ, 781, 54
Rugheimer, S., & Kaltenegger, L. 2018, ApJ, 854, 19
Rugheimer, S., Kaltenegger, L., Zsom, A., et al. 2013, AsBio, 13, 251
Sagan, C., Thompson, W. R., Carlson, R., et al. 1993, Natur, 365, 715
Segura, A., Kasting, J. F., Meadows, V., et al. 2005, AsBio, 5, 706
Segura, A., Meadows, V. S., Kasting, J. F., et al. 2007, A&A, 472, 665
Sharpe, S. W., Johnson, T. J., Sams, R. L., et al. 2004, ApSpe, 58, 1452
Snellen, I., de Kok, R., Le Poole, R., et al. 2013, ApJ, 764, 182
Som, S. M., Catling, D. C., Harnmeijer, J. P., Polivka, P. M., & Buick, R. 2012, Natur, 484, 359
Stevenson, K. B., Lewis, N. K., Bean, J. L., et al. 2016, PASP, 128, 094401
Torres, G., Kipping, D. M., Fressin, F., et al. 2015, ApJ, 800, 99
Traub, W. A., & Jucks, K. 2002, in Atmospheres in the Solar System: Comparative Aeronomy. Geophysical Monograph Vol. 130, ed. M. Mendillo, A. Nagy, & J. H. Waite (Washington, DC: AGU), 369
Traub, W. A., & Stier, M. T. 1976, ApOpt, 15, 364
Udry, S., Bonfils, X., Delfosse, X., et al. 2007, A&A, 469, L43
Vidal-Madjar, A., Arnold, A., Ehrenreich, D., et al. 2010, A&A, 523, A57
Wagner, G., & Birk, M. 2003, JQSRT, 82, 443
Walker, J. C. G. 1977, Evolution of the Atmosphere (New York: Macmillan)
Zahnle, K., Arndt, N., Cockell, C., et al. 2007, SSRv, 129, 35